



High quality, high index-contrast chalcogenide microdisk resonators

RIZHEN ZHANG,^{1,2} ZHEN YANG,^{1,2} MINGYUE ZHAO,^{1,2} PEIPENG XU,^{1,2,7}  WEI ZHANG,^{1,2}  ZHE KANG,^{3,4} JIAJIU ZHENG,⁵  SHIXUN DAI,^{1,2} RONGPING WANG,^{1,2,8}  AND ARKA MAJUMDAR^{5,6} 

¹Faculty of Electrical Engineering and Computer Science, Ningbo University, Ningbo 315211, China

²Key Laboratory of Photoelectric Detection Materials and Devices of Zhejiang Province, Ningbo 315211, China

³Ningbo Research Institute, Zhejiang University, Ningbo 315100, China

⁴Centre for Optical and Electromagnetic Research, National Engineering Research Center for Optical Instruments, Zhejiang University, Hangzhou 310058, China

⁵Department of Electrical and Computer Engineering, University of Washington, Seattle, WA 98195, USA

⁶Department of Physics, University of Washington, Seattle, WA 98195, USA

⁷xupeipeng@nbu.edu.cn

⁸wangrongping@nbu.edu.cn

Abstract: We demonstrate the high quality (Q) factor microdisk resonators in high index-contrast chalcogenide glass (ChG) film GeSbSe using electron-beam lithography followed by plasma dry etching. High confinement, low-loss, and single-point-coupled microdisk resonators with a loaded Q factor of 5×10^5 are measured. We also present pulley-coupled microdisk resonators for relaxing the requirements on the coupling gap. While adjusting the wrap-around coupling waveguides to be phase-matched to the resonator mode, a single specific microdisk radial mode can be excited. Moreover, the thermal characterization of microdisk resonators is carried out to estimate the thermo-optic coefficient of $6.7 \times 10^{-5}/\text{K}$ for bulk ChG.

© 2021 Optical Society of America under the terms of the [OSA Open Access Publishing Agreement](#)

1. Introduction

High quality (Q) factor optical resonators, with the capability of trapping light in a tiny volume for long periods [1], are in high demand for many applications, such as optical sensing [2,3], cavity optomechanics [4], optical data processing [5], ultralow threshold lasers [6–8], optical modulators [9], and nonlinear optics [10]. Two different resonator structures, namely photonic crystal cavities [11,12] and whispering gallery mode (WGM) resonators (microrings [13], microdisks [14,15]), are used extensively used in the planar, integrated photonic circuits, among which microdisk resonators demonstrate higher quality factors due to less scattering because of only one etched sidewall [14]. To further promote the potential of the microdisk resonators, significant interest has been focused on developing microdisks on various material platforms, such as silicon dioxide [16], silicon carbide [17], lithium niobate [18,19], and even polymers [20].

As one of the important infrared optical material, chalcogenide glasses (ChGs) exhibit very attractive material properties [21]. They have very low linear absorption loss over a wide wavelength range (from the visible around 0.5 μm , to mid-infrared wavelengths, up to 20 μm) with a relatively high refractive index ($n=2\sim 3$), enabling a small optical mode volume without excessive radiative loss. Besides, ChGs exhibit exceptionally high optical nonlinearity (Kerr, Raman, and Brillouin coefficients) which is two or three orders of magnitude greater than silica and comparable or superior to silicon [22,23]. Moreover, ChGs have excellent scalability that could be easily deposited on any substrates using low-cost, large-area techniques such as evaporation and sputtering [24,25]. Benefiting from these excellent properties, ChGs has been

promising in infrared optical resonators for cavity-enhanced chemical and biological sensors due to the fact that most of the molecules have characteristic absorption bands in the infrared [26–28]. Microdisk resonators in thermally evaporated As_2S_3 and $\text{Ge}_{23}\text{Sb}_7\text{S}_{70}$ ChGs film have been developed successfully with a high Q factor and medium index-contrast [29,30]. However, the fabrication technologies in a relatively high index-contrast ChGs platform ($n_{\text{cav}}/n_{\text{bg}} \sim 2$) are still in the infancy, resulting in the difficulty in achieving high Q factor. High index-contrast microresonators yield smaller mode volume, thus much stronger linear and nonlinear interaction and more flexible dispersion tailoring ability. Considering the rich potential on linear and nonlinear applications, it is of great interest to develop versatile high index-contrast ChGs microresonators.

In this work, utilizing a high index-contrast and nontoxic $\text{Ge}_{28}\text{Sb}_{12}\text{Se}_{60}$ (GeSbSe) film [12], we report the fabrication of high Q factor microdisk resonators using electron-beam lithography following by plasma dry etching. We demonstrated planar microdisk resonators with a loaded Q factor of $\sim 5 \times 10^5$ when the access waveguide is side-coupled to the resonator at a single point. In this case, the critical coupling is experimentally achieved for the 3rd order radial mode. To release the requirements on the coupling gap, we also demonstrate the pulley-coupled microdisk resonators [29]. While adjusting the pulley waveguide width to be phase-matched to the mode of resonator, single-mode operation of specific mode of the microdisk can be conveniently achieved. Finally, the thermal characterization of microdisk resonators is carried out to estimate the thermal drift of the device.

2. Device fabrication and measurement

We fabricated planar integrated microdisk resonators with an access waveguide. First, 300 nm thick GeSbSe films were thermally evaporated from GeSbSe glass powder (prepared by melt quenching in a quartz ampoule) onto 4" silicon wafers with 3- μm thermal oxide layer as a bottom cladding. The refractive index of the ChG film was determined to be ~ 2.8 at a wavelength of 1550 nm using ellipsometry, enabling high index-contrast devices. Then a 30 nm thick of SiO_2 film was directly deposited on GeSbSe by magnetron sputtering at room temperature. The SiO_2 film was used to protect chalcogenide films from damages during the development and reduce the sidewall roughness during the etching. The device pattern was defined by direct-writing 30 keV electron-beam lithography (Raith eLINE Plus) using a positive tone AR-P 6200 resist. To remove residues during the development process which leads to micro-masking formation in fluorine-based etching, the exposed structures underwent a plasma treatment step with $\text{O}_2/\text{Ar}/\text{CHF}_3$ gases (see parameters in "Before etching" column in Table 1). The pattern was then transferred onto the underlying ChGs layer by an anisotropic etching via an inductively coupled plasma (ICP) process utilizing a gas mixture of CHF_3 and CF_4 . The etching recipes, including gas flow rate, chamber pressure, radiofrequency (RF) power, and etching gas ratio (for the fluorine chemistry), were investigated to determine the best performance (see parameters in "Etching" column in Table 1). Following etching, another optimized plasma treatment was performed on the sample to remove the fluorocarbon polymer deposited on the waveguide sidewalls (see parameters in "Removing" in Table 1). Finally, the remaining photoresists were stripped by soaking the sample in N-methyl-2-pyrrolidone (NMP) for 2 hours.

Figure 1(a) shows a scanning electron microscopy (SEM) image of the fabricated microdisk resonator with a radius of 45 μm . The resonators are coupled to an access waveguide to allow the optical characterization in transmission measurements. The zoomed-in view of the coupling region in the yellow frame in Fig. 1(a) is shown in Fig. 1(b). Compared with the taper fiber coupling configuration, access waveguide coupling is preferred in the on-chip photonic integrated circuits, and this can improve the stability and durability of our device. Fully etched fiber-waveguide grating couplers are also fabricated to facilitate coupling light to the waveguide from an external fiber, as shown in Fig. 1(c). The grating coupler has a fixed duty cycle of $\sim 70\%$

Table 1. Summary of optimized etching recipes for a ChGs microdisk resonator.

Parameters	Before etching	Etching	Removing
O ₂ flow rate (sccm)	30	0	30
Ar flow rate (sccm)	2	0	2
CHF ₃ flow rate (sccm)	3	20	3
CF ₄ flow rate (sccm)	0	10	0
RF power (W)	10	100	30
ICP power (W)	200	300	300
Pressure (mTorr)	10	6	10

and a period of 0.92 μm , which is aligned to the single-mode fibers (SMFs) at an incident angle of 12°. The peak coupling efficiency for the regular full-etched grating coupler is measured to be $\sim 10\%$, which can be further improved using a sub-wavelength grating coupler [31].

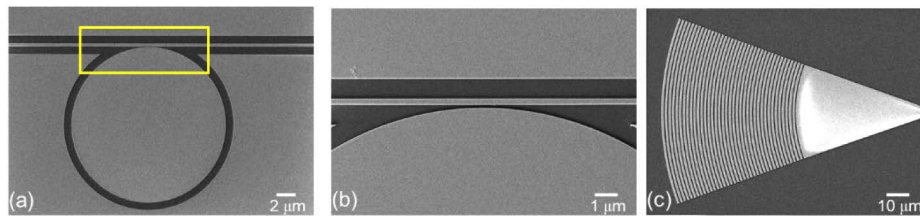


Fig. 1. (a) Scanning Electron Microscopy (SEM) image of a ChG microdisk resonator coupled to an access waveguide. The disk diameter is 45 μm . (b) Zoomed-in view of the structure at the waveguide-resonator coupling region. (c) SEM image of the TE mode grating coupler.

In the experiments, light with sub-MHz linewidth from the tunable laser (Santac TSL-550) is coupled to the waveguide via focusing grating couplers and collected on the other side of the waveguides into a low-noise power meter (Santec MPM210) via SMFs. The power of the coupled light was kept low enough ($< 100 \mu\text{W}$) to minimize the thermo-optic effects of the ChGs [32]. The polarization of the input light was controlled to match the fundamental quasi-TE mode of the waveguide by a manual fiber polarization controller (Thorlabs FPC526). The experimental temperature was fixed at 20°C using a thermoelectric controller to avoid any thermal shift of the resonators.

3. Results and discussion

3.1. Performance of the single-point-coupled microdisk resonators

Figure 2(a) shows the representative output spectrum of the fabricated resonators with a radius of 45 μm . The waveguide width is 720nm, enabling a single mode operation, while the coupling gap is 190 nm. The loaded Q factors at all resonances from 1520 nm to 1580 nm are extracted, and a histogram of device performance from multiple resonances over our sample is shown in Fig. 2(b). All the first few radial mode orders observed in the experiment exhibit a $Q > 10^5$. In Fig. 2(c), the full width at half maximum (FWHM), denoted as $\Delta\lambda$, was measured to be 3.15 pm by a Lorentzian fitting. Based on the formula $Q = \lambda/\Delta\lambda$, the loaded Q factor of $\sim 5 \times 10^5$ is calculated at 1559.657 nm. To understand the resonant mode, we calculate the transverse electric (TE) polarized mode profile of the resonator in the axisymmetric ChG microdisk membrane using the finite element method (FEM) as shown in the inset of Fig. 2(c) (COMSOL Multiphysics).

According to the free spectral region (FSR) in different radial modes, the radial and azimuthal order for the resonant mode is identified to be 1 and 412, respectively. One of the properties in the traveling-wave resonators such as microdisk is resonance mode splitting due to the coupling between the degenerate clockwise (CW) and counterclockwise (CCW) modes (usually comes from the sidewall roughness scattering). In our case, we can also observe a typical resonance spectrum with a mode splitting of $\delta\lambda = 2.9$ pm (see Fig. 2(d)), which can be potentially used to detect nanoparticles at a single-particle resolution [33].

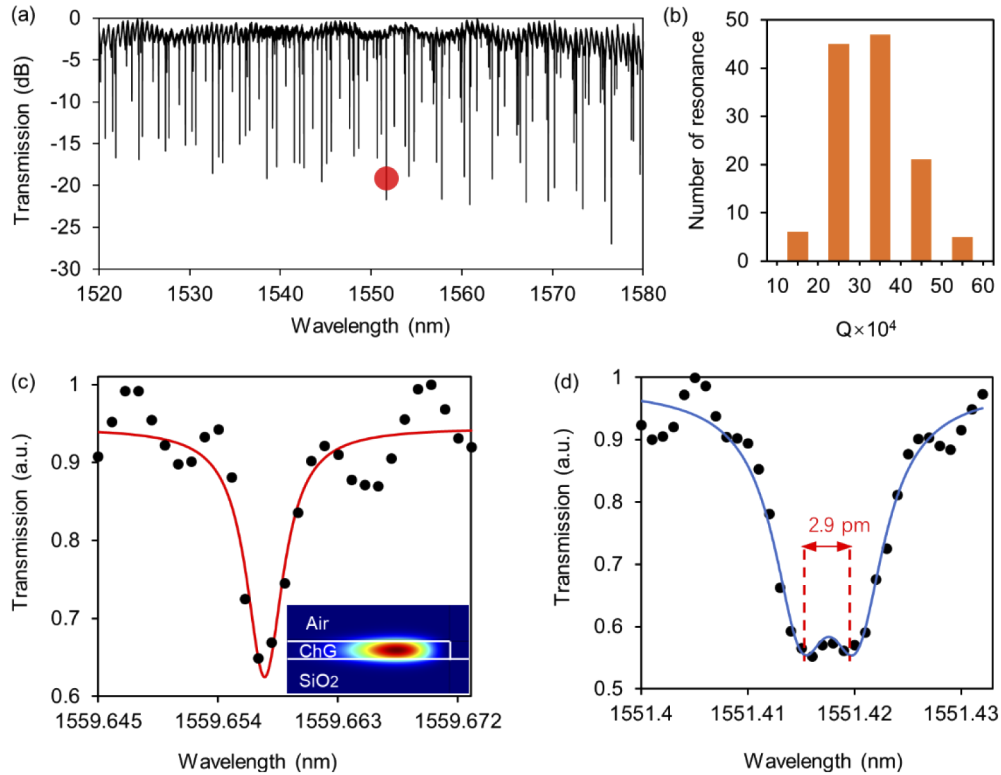


Fig. 2. (a) Transmission spectrum of a ChG microdisk resonator with a radius of 45 μm . (b) Histogram of extracted loaded Q factor at each resonant wavelength. (c) A high Q factor of $\sim 5 \times 10^5$ is observed at $\lambda = 1559.657$ nm. Inset: the fundamental TE mode profile of ChG resonator. (d) A zoomed view of one of the resonances in (a), wherein the resonance shows mode splitting due to the coupling between the degenerate CW and CCW modes of the resonator.

Among the excited radial order modes in microdisk, the first-order mode, as show in Fig. 2(c), is regarded as one of the most significant mode as they exhibit high Q factor and low mode volume. Since microdisk is a traveling-wave-resonator, in the weak coupling regime, the all-pass transmission and the loaded Q factor (Q_L) at resonance are respectively given by [14],

$$T = \frac{P_{\text{out}}}{P_{\text{in}}} = \left| \frac{1 - Q_0/Q_c}{1 + Q_0/Q_c} \right|^2, \quad (1)$$

$$Q_L^{-1} = Q_0^{-1} + Q_c^{-1}, \quad (2)$$

where Q_0 and Q_c are respectively the intrinsic and coupling quality factor, Q_0 is calculated to be $\sim 5.6 \times 10^5$ at the resonance wavelength of 1559.657 nm when substituting the power transmission

of ~ 0.62 into Eq. (2). The intrinsic Q_0 is limited by several loss mechanisms, namely absorption, radiation, and scattering

$$Q_0^{-1} = Q_r^{-1} + Q_m^{-1} + Q_s^{-1}, \quad (3)$$

where Q_r , Q_m and Q_s denotes the intrinsic radiative loss, material absorption loss, scattering loss due to surface inhomogeneities, respectively. Q_r^{-1} vanishes exponentially with increasing size, so with $R > 15 \mu\text{m}$, $Q_r > 10^{15}$ (R is the microdisk radius), Q_m was calculated to be 1.89×10^6 , which is derived from the reported linear attenuation of 0.3 dB/cm in bulk $\text{Ge}_{28}\text{Sb}_{12}\text{Se}_{60}$ glass [34]. Our measured loaded Q factors are smaller than both Q_r and Q_m , suggesting that the Q factor is limited by the scattering loss from the surface and edge of the resonators. From the measured spectrum of the microdisk resonator, we also find that the near-critical coupling occurs near 1550 nm for several families of modes (quoted for resonant peaks with extinction ratios > 20 dB). The full width at half maximum (FWHM) of 5.83 pm and the measured high loaded Q factor is $\sim 2.7 \times 10^5$ at $\lambda = 1551.693$ nm (the resonances at the solid red circle in Fig. 2(a)). We can calculate the intrinsic Q factor of 5.4×10^5 since it is simply twice the measured loaded Q factor. The resonant mode in near-critical coupling is determined to be the 3rd order radial mode of the microdisk, referring to our simulation results.

3.2. Performance of the pulley-coupled microdisk resonators

When the waveguide is side-coupled to the resonator at a single point, the critical coupling condition requires a very narrow coupling gap between the waveguide and the resonator [35]. In contrast, the pulley geometry allows for relaxing the coupling gap requirements by increasing the coupling length. Moreover, while adjusting the pulley waveguide width to be phase-matched to the resonator mode, the single-mode operation of the microdisk can be expected. Figure 3(a) shows the normalized transmission spectrum of a $32 \mu\text{m}$ -radius ChG-microdisk side coupled to a waveguide with the coupling in a single-point configuration. One can find that several radial TE modes of the microdisk resonator are excited at the same time. The width of the access waveguide width is 720 nm, and the coupling gap is 150 nm. We also examine the same microdisk transmission spectrum when a pulley coupler is employed (see Fig. 3(b)), which features a series of discrete, equally spaced resonant peaks. In this case, only one single mode of the resonator is excited while the other radial modes are uncoupled from the waveguide field. The coupling length is the half circumference of the ChG-microdisk, and the coupling gap is 290 nm, which is almost twice that in a single-point coupling scheme. Compared to single point couplers, these features are within the reach of current deep-UV lithography systems, and thus can be fabricated using high throughput photo-lithography systems in a foundry. Figure 3(c) shows a typical resonance with a high Q factor of 3.7×10^5 at the wavelength of 1537.467 nm by Lorentzian fitting. According to the microdisk resonator simulations, this resonance corresponds to the 2nd radial order mode with azimuthal number of 286 and an FSR of 4.5 nm. Such pulley-coupled microdisk resonators possess advantages of a wider waveguide-resonator gap, and single-mode operation, thus making them an excellent candidate for applications where a strong light-matter interaction is required.

Figure 3(d) shows the pulley coupling configuration in this work. The first-order temporal perturbation theory gives the coupling coefficient between a waveguide and an adjacent resonator as [15]

$$\kappa = S \int_{-\theta_0}^{\theta_0} e^{i\theta(\kappa_0 n_{\text{wg}} R_{\text{wg}} - m)} d\theta = 2\theta_0 \text{sinc} \left[(\kappa_0 n_{\text{wg}} R_{\text{wg}} - m) \frac{\theta_0}{\pi} \right], \quad (4)$$

where S is a parameter independent of θ , θ_0 is the angular range of the wrap-around coupling, $k_0 = 2\pi/\lambda_0$ is the wavenumber in the free space, and m is the azimuthal mode order of the resonator. The effective radius of the curved waveguide (R_{wg}) is larger than the radius of the disk ($R_{\text{wg}} = R_{\text{disk}} + g + w/2$). We note that the phase mismatching $(\kappa_0 n_{\text{wg}} R_{\text{wg}} - m)\theta_0$ between the two

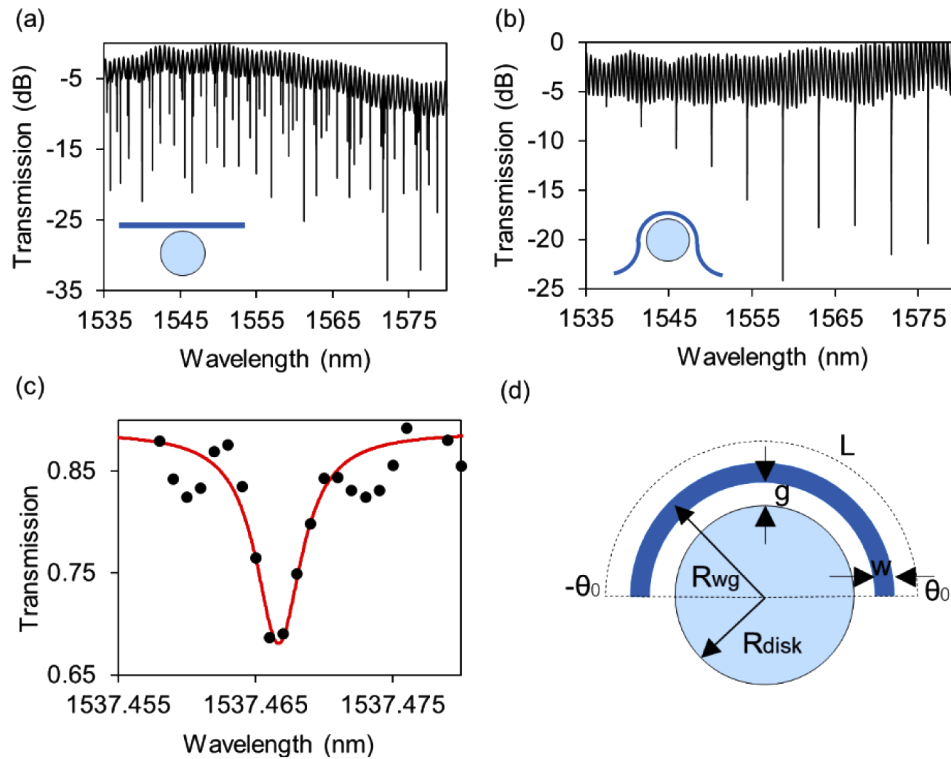


Fig. 3. (a) The normalized transmission spectrum of a 32-micron-radius ChG microdisk side coupled to a waveguide with a single point coupling scheme. (b) The normalized transmission of the waveguides coupled to the same microdisk in the pulley configuration. (c) Measured spectrum and Lorentzian fitting around the resonant wavelength at 1537.467 nm, the measured loaded Q-factor is $\sim 3.7 \times 10^5$. (d) The geometry of the pulley structure used in this work.

structures can reduce the coupling coefficient considerably. If the phase-matching condition is met ($k_0 n_{wg} R_{wg} = m$), the coupling coefficient is a linear function of the coupling length (which is proportional to θ_0). The phase-matching condition is highly dependent on the exciting radial modes of the microdisk resonator. Since the effective index of each radial mode is defined as ($n_{disk} \equiv m/k_0 R_{disk}$), the phase-matching condition can be satisfied at $n_{wg} R_{wg} = n_{disk} R_{disk}$. When the waveguide width is chosen to be 720 nm in our case, only the 2nd radial order mode of the disk is excited. The strict phase-matching condition does not allow the other radial modes of the microdisk to have significant coupling to the waveguide, verified by the achieved transmission spectrum as shown in Fig. 3(b). To achieve fundamental mode excitation in the resonator, waveguide width need to be enlarged given the increase of the n_{disk} .

3.3. Thermal characteristics on the ChG microdisk

We finally investigate the thermal characteristics of the proposed ChG microdisk resonators. In the experiment, a thermoelectric controller (TEC) is placed beneath the chip to control the temperature of the substrate. Figure 4(a) shows the measured transmission spectrum of the fabricated microdisk at the ambient temperature changing from 35°C to 55°C with a step of 5°C. From this figure, we can find a redshift of the resonant wavelength for the microdisk with increasing ambient temperature. Figure 4(b) shows a linear correlation between the wavelength drift and the temperature change, indicating a redshift of approximately 69 pm when the ambient

temperature is increased by 1 K. Such a linear relationship originates from the thermo-optic effect and thermal expansion, which can be calculated using the temperature dependence equation [17],

$$\frac{d\lambda}{dT} = \lambda_0 \left(\frac{1}{n_{\text{eff}}} \frac{dn_{\text{eff}}}{dT} + \frac{1}{D} \frac{dD}{dT} \right) = \lambda_0 \left(\frac{C_{TOC}}{n_0} + C_{CTE} \right), \quad (5)$$

where λ_0 is the resonant wavelength, n_{eff} is the effective index of resonant mode, and D is the principal diameter of the microdisk. As our proposed resonator provides a good confinement of the optical mode in ChG layer (see the inset of Fig. 2(c)), the temperature dependence of effective index of optical mode is primarily determined by the thermo-optic coefficient of material, $(1/n_0)(dn_0/dT) = (1/n_{\text{eff}})(dn_{\text{eff}}/dT)$, where n_0 is the refractive index of bulk ChG. Using the thermal expansion coefficient C_{CTE} of $1.4 \times 10^{-5}/\text{K}$ for GeSbSe glass at room temperature [32] and our experimental results of $d\lambda/dT = 69 \text{ pm/K}$, the thermo-optic coefficient C_{TOC} is estimated from Eq. (5), being $6.7 \times 10^{-5}/\text{K}$, which is in excellent agreement with those published results [32]. One can also figure out from Eq. (5) and these parameters that, the thermal expansion factor has a smaller contribution to the geometry change in the resonance shift compared with the thermo-optic effect in GeSbSe glass.

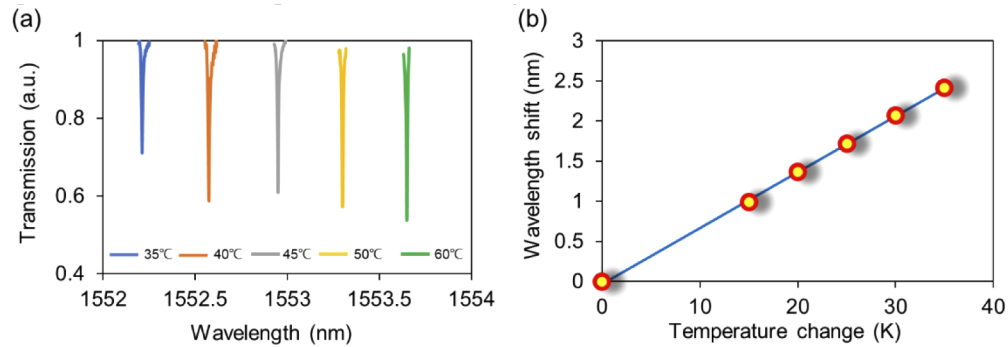


Fig. 4. (a) Transmission vs. wavelength for a resonant mode in the microdisk with a radius of $45 \mu\text{m}$ at various temperatures. (b) Redshift in resonant wavelength of optical mode as a function of temperature. A linear fit to the data yields $d\lambda/dT$ of 69 pm/K .

4. Conclusion

In summary, we report high index-contrast ChG microdisk resonators in the near-infrared region. Plasma treatment and optimized fluorine etching recipes are employed to produce low-loss devices. Planar microdisk resonators with a loaded high Q factor of $\sim 5 \times 10^5$ for the first-order mode are demonstrated when the access waveguide is side-coupled to the resonator at a single point. We also present pulley-coupled microdisk resonators with larger coupling gaps when the waveguide wraps around the resonator. By choosing the proper width for the wrapped waveguide and making the phase matching to the mode of resonator, single-mode operation of the microdisk can be realized. The thermal responses are experimentally investigated under different temperatures, and the demonstrated temperature drift in the device is 69 pm/K . The availability of such high index-contrast ChGs microdisk resonators with high Q factor, easy fabrication, and single-mode operation will find numerous applications for optical sensing, optical signal processing, and nonlinear photonics.

Funding. National Natural Science Foundation of China (61875099, 62075188, 61775109); Natural Science Foundation of Zhejiang Province (LGJ18F050001, LY18F050005, LY21F050007); Natural Science Foundation of Ningbo (202003N4007); National Key Research and Development Program of China (2020YFB1805900); 3315 Innovation Team in Ningbo City; ONR-YIP Award; Ningbo University (K.C. Wong Magna Fund).

Acknowledgments. The authors thank Pengxin Chen for the grating coupler measurements.

Disclosures. The authors declare no conflicts of interest.

Data availability. Data underlying the results presented in this paper are not publicly available at this time but may be obtained from the authors upon reasonable request.

References

1. K. J. Vahala, "Optical microcavities," *Nature* **424**(6950), 839–846 (2003).
2. A. M. Armani, R. P. Kulkarni, S. E. Fraser, R. C. Flagan, and K. J. Vahala, "Label-Free, Single-Molecule Detection with Optical Microcavities," *Science* **317**(5839), 783–787 (2007).
3. J. Liao and L. Yang, "Optical whispering-gallery mode barcodes for high-precision and wide-range temperature measurements," *Light: Sci. Appl.* **10**(1), 32 (2021).
4. M. Eichenfield, J. Chan, R. M. Camacho, K. J. Vahala, and O. Painter, "Optomechanical crystals," *Nature* **462**(7269), 78–82 (2009).
5. W. Zhang and J. Yao, "Photonic integrated field-programmable disk array signal processor," *Nat. Commun.* **11**(1), 406 (2020).
6. B. Ellis, M. A. Mayer, G. Shambat, T. Sarmiento, J. Harris, E. E. Haller, and J. Vučković, "Ultralow-threshold electrically pumped quantum-dot photonic-crystal nanocavity laser," *Nat. Photonics* **5**(5), 297–300 (2011).
7. S. M. Spillane, T. J. Kippenberg, and K. J. Vahala, "Ultralow-threshold Raman laser using a spherical dielectric microcavity," *Nature* **415**(6872), 621–623 (2002).
8. Y. Zhang, M. Khan, Y. Huang, J. Ryou, P. Deotare, R. Dupuis, and M. Lončar, "Photonic crystal nanobeam lasers," *Appl. Phys. Lett.* **97**(5), 051104 (2010).
9. M. Li, J. Ling, Y. He, U. A. Javid, S. Xue, and Q. Lin, "Lithium niobate photonic-crystal electro-optic modulator," *Nat. Commun.* **11**(1), 4123 (2020).
10. A. L. Gaeta, M. Lipson, and T. J. Kippenberg, "Photonic-chip-based frequency combs," *Nat. Photonics* **13**(3), 158–169 (2019).
11. Y. Akahane, T. Asano, B.-S. Song, and S. Noda, "High-Q photonic nanocavity in a two-dimensional photonic crystal," *Nature* **425**(6961), 944–947 (2003).
12. M. Zhao, Z. Yang, R. Zhang, J. Zheng, P. Xu, W. Zhang, S. Dai, R. Wang, and A. Majumdar, "High Q chalcogenide photonic crystal nanobeam cavities," *IEEE Photonics Technol. Lett.*, 1 (2021).
13. W. Bogaerts, P. De Heyn, T. Van Vaerenbergh, K. De Vos, S. Kumar Selvaraja, T. Claes, P. Dumon, P. Bienstman, D. Van Thourhout, and R. Baets, "Silicon microring resonators," *Laser Photonics Rev.* **6**(1), 47–73 (2012).
14. M. Soltani, S. Yegnanarayanan, and A. Adibi, "Ultra-high Q planar silicon microdisk resonators for chip-scale silicon photonics," *Opt. Express* **15**(8), 4694–4704 (2007).
15. E. S. Hosseini, S. Yegnanarayanan, A. H. Atabaki, M. Soltani, and A. Adibi, "Systematic design and fabrication of high-Q single-mode pulley-coupled planar silicon nitride microdisk resonators at visible wavelengths," *Opt. Express* **18**(3), 2127–2136 (2010).
16. T. J. Kippenberg, S. M. Spillane, D. K. Armani, and K. J. Vahala, "Fabrication and coupling to planar high-Q silica disk microcavities," *Appl. Phys. Lett.* **83**(4), 797–799 (2003).
17. X. Lu, J. Y. Lee, P. X. L. Feng, and Q. Lin, "Silicon carbide microdisk resonator," *Opt. Lett.* **38**(8), 1304–1306 (2013).
18. C. Wang, M. J. Burek, Z. Lin, H. A. Atikian, V. Venkataraman, I. C. Huang, P. Stark, and M. Lončar, "Integrated high quality factor lithium niobate microdisk resonators," *Opt. Express* **22**(25), 30924–30933 (2014).
19. R. Wu, J. Zhang, N. Yao, W. Fang, L. Qiao, Z. Chai, J. Lin, and Y. Cheng, "Lithium niobate micro-disk resonators of quality factors above 107," *Opt. Lett.* **43**(17), 4116–4119 (2018).
20. C. Lemieux-Leduc, R. Guertin, M.-A. Bianki, and Y.-A. Peter, "All-polymer whispering gallery mode resonators for gas sensing," *Opt. Express* **29**(6), 8685–8697 (2021).
21. B. J. Eggleton, B. Luther-Davies, and K. Richardson, "Chalcogenide photonics," *Nat. Photonics* **5**(3), 141–148 (2011).
22. Y. Yu, X. Gai, P. Ma, K. Vu, Z. Yang, R. Wang, D.-Y. Choi, S. Madden, and B. Luther-Davies, "Experimental demonstration of linearly polarized 2–10 μm supercontinuum generation in a chalcogenide rib waveguide," *Opt. Lett.* **41**(5), 958–961 (2016).
23. B. J. Eggleton, C. G. Poulton, and R. Pant, "Inducing and harnessing stimulated Brillouin scattering in photonic integrated circuits," *Adv. Opt. Photonics* **5**(4), 536–587 (2013).
24. G. Kang, M. R. Krogstad, M. Grayson, D.-G. Kim, H. Lee, J. T. Gopinath, and W. Park, "High quality chalcogenide-silica hybrid wedge resonator," *Opt. Express* **25**(13), 15581–15589 (2017).
25. H. Lin, Y. Song, Y. Huang, D. Kita, S. Deckoff-Jones, K. Wang, L. Li, J. Li, H. Zheng, Z. Luo, H. Wang, S. Novak, A. Yadav, C.-C. Huang, R.-J. Shiue, D. Englund, T. Gu, D. Hewak, K. Richardson, J. Kong, and J. Hu, "Chalcogenide glass-on-graphene photonics," *Nat. Photonics* **11**(12), 798–805 (2017).
26. J. Hu, N. Carlie, L. Petit, A. Agarwal, K. Richardson, and L. C. Kimerling, "Cavity-Enhanced IR Absorption in Planar Chalcogenide Glass Microdisk Resonators: Experiment and Analysis," *J. Lightwave Technol.* **27**(23), 5240–5245 (2009).

27. P. Ma, D.-Y. Choi, Y. Yu, Z. Yang, K. Vu, T. Nguyen, A. Mitchell, B. Luther-Davies, and S. Madden, "High Q factor chalcogenide ring resonators for cavity-enhanced MIR spectroscopic sensing," *Opt. Express* **23**(15), 19969–19979 (2015).
28. Z. Han, P. Lin, V. Singh, L. Kimerling, J. Hu, K. Richardson, A. Agarwal, and D. T. H. Tan, "On-chip mid-infrared gas detection using chalcogenide glass waveguide," *Appl. Phys. Lett.* **108**(14), 141106 (2016).
29. J. Hu, N. Carlie, N.-N. Feng, L. Petit, A. Agarwal, K. Richardson, and L. Kimerling, "Planar waveguide-coupled, high-index-contrast, high-Q resonators in chalcogenide glass for sensing," *Opt. Lett.* **33**(21), 2500–2502 (2008).
30. Q. Du, Y. Huang, J. Li, D. Kita, J. Michon, H. Lin, L. Li, S. Novak, K. Richardson, W. Zhang, and J. Hu, "Low-loss photonic device in Ge–Sb–S chalcogenide glass," *Opt. Lett.* **41**(13), 3090–3093 (2016).
31. Y. Wang, X. Wang, J. Flueckiger, H. Yun, W. Shi, R. Bojko, N. A. F. Jaeger, and L. Chrostowski, "Focusing sub-wavelength grating couplers with low back reflections for rapid prototyping of silicon photonic circuits," *Opt. Express* **22**(17), 20652–20662 (2014).
32. Schott Infrared Chalcogenide Glasses Datasheet, http://www.schott.com/d/advanced_optics/a8acc8e2-8855-4be6-8b2a-e4b2ada72a15/1.0/schott-infrared-chalcog-glasses-irg25-january-2016-eng.pdf
33. J. Zhu, S. K. Ozdemir, Y.-F. Xiao, L. Li, L. He, D.-R. Chen, and L. Yang, "On-chip single nanoparticle detection and sizing by mode splitting in an ultrahigh-Q microresonator," *Nat. Photonics* **4**(1), 46–49 (2010).
34. M. R. Krogstad, S. Ahn, W. Park, and J. T. Gopinath, "Optical Characterization of Chalcogenide Ge–Sb–Se Waveguides at Telecom Wavelengths," *IEEE Photonics Technol. Lett.* **28**(23), 2720–2723 (2016).
35. A. Yariv, "Universal relations for coupling of optical power between microresonators and dielectric waveguides," *Electron. Lett.* **36**(4), 321–322 (2000).